Stacking-engineered ferroelectricty and multiferroic order in van der Waals magnets

Daniel Bennett,[1,*] Gabriel Martínez-Carracedo,[2,3] Xu He,[4] Jaime Ferrer,[2,3] Philippe Ghosez,[4] Riccardo Comin,[5] and Efthimios Kaxiras[1,6]

[1]*John A. Paulson School of Engineering and Applied Sciences, Harvard University, Cambridge, Massachusetts 02138, USA*
[2]*Departamento de Física, Universidad de Oviedo, 33007 Oviedo, Spain*
[3]*Centro de Investigación en Nanomateriales y Nanotecnología, Universidad de Oviedo-CSIC, 33940 El Entrego, Spain*
[4]*Theoretical Materials Physics, Q-MAT, University of Liège, B-4000 Sart Tilman, Belgium*
[5]*Department of Physics, Massachusetts Institute of Technology, Cambridge, MA, USA*
[6]*Department of Physics, Harvard University, Cambridge, Massachusetts 02138, USA*

Two-dimensional (2D) materials that exhibit spontaneous magnetization, polarization or strain (referred to as ferroics) have the potential to revolutionize nanotechnology by enhancing the multifunctionality of nanoscale devices. However, multiferroic order is difficult to achieve, requiring complicated coupling between electron and spin degrees of freedom. We propose a universal method to engineer multiferroics from van der Waals magnets by taking advantage of the fact that changing the stacking between 2D layers can break inversion symmetry, resulting in ferroelectricity as well as magnetoelectric coupling. We illustrate this concept using first-principles calculations in bilayer NiI_2, which can be made ferroelectric upon rotating two adjacent layers by 180° with respect to the bulk stacking. Furthermore, we discover a novel strong magnetoelectric coupling between the interlayer spin order and interfacial electronic polarization. Our approach is not only general but also systematic, and can enable the discovery of a wide variety of 2D multiferroics with strong magnetoelectric coupling.

Introduction.—The ability to synthesize stable layered van der Waals (vdW) materials has opened up new possibilities for mechanically-assembled stacks of heterostructures and led to significant advances in materials science [1–3]. These new artificial materials display a range of unprecedented multifunctional properties [4–6], one notable example being ferroic orders such as ferromagnetism [7, 8] and ferrroelectricity [9–11]. 2D magnetic materials show great promise as a new class of magnets because their properties can be controlled through the application of external stimuli beyond temperature and magnetic field, such as mechanical strain or gate voltage [12–15]. Recently a new type of ferroelectricity in vdW materials was proposed [9] and experimentally observed [10, 11, 16–20]. For vdW materials such as hexagonal boron nitride (hBN) or transition metal dichalcogenides (TMDs) where centrosymmetry is broken by stacking-engineering, an electronic out-of-plane polarization $P_\perp$ occurs through interlayer charge transfer. The magnitude and orientation of $P_\perp$ is determined by the relative stacking between the layers and can be switched by a relative sliding, resulting in 'vdW ferroelectricity' [11, 21, 22].

The functional properties of vdW materials can be further tuned by introducing a relative twist or lattice mismatch between neighboring layers, resulting in a moiré superlattice on a scale much larger than the underlying crystal periodicity. This has been the source of many interesting and unconventional emergent phenomena, one notable example being superconductivity in 'magic angle' twisted bilayer graphene [23–26]. Creating a moiré superlattice from a vdW ferroelectric results in the formation of moiré polar domains (MPDs) [27, 28]. These MPDs have been experimentally shown to result in ferroelectricity [11, 18] through the asymmetric change in domain size in response to an applied electric field. The MPDs also have an in-plane polarization component $\mathbf{P}_\parallel$ and as a result they have nontrivial topology [29–32], analogous to the polar textures observed in oxide perovskites [33–36]. Similar topological magnetic textures have been proposed and reported by twisting vdW magnets, such as CrI_3 [37, 38].

The coexistence or interplay between ferroelectricity and magnetism can give rise to multiferroic order [39, 40], which is promising for enhanced functionality in nanodevices. While 2D multiferroics are less common than bulk counterparts such as $BiFeO_3$ [41], the vdW magnet NiI_2 [42–44] has shown signals of multiferroic order down to the monolayer limit [45]. The proposed mechanism in NiI_2 is the appearance of improper ferroelectricity in response to long-range magnetic order which breaks inversion symmetry [38, 46–49]. There are a few disadvantages to this relatively complicated magnetoelectric coupling mechanism. The strength of the coupling depends on the strength of the Rashba spin-orbit coupling (SOC) in a material and may be weak in materials that do not contain heavy elements. Moreover, it also requires magnetization gradients such as complex spin textures.

While the coexistence of ferroic orders has previously been predicted in other vdW magnets [9, 50–52], significant coupling between polarization and magnetization, which would enhance multifunctionality [39], is not guaranteed. Here we discover a novel strong magnetoelectric coupling in artificially stacked vdW magnets, between the interlayer electronic polarization and spin ordering. In the model system we use to illustrate this effect, NiI_2, we find that changing the interlayer spin order modifies the electronic structure and can change the electronic polarization by a factor of two; this in turn leads to additional jumps in the ferroelectric hysteresis loop, implying that ferroelectric polarization may be tuned using a magnetic

* dbennett@seas.harvard.edu

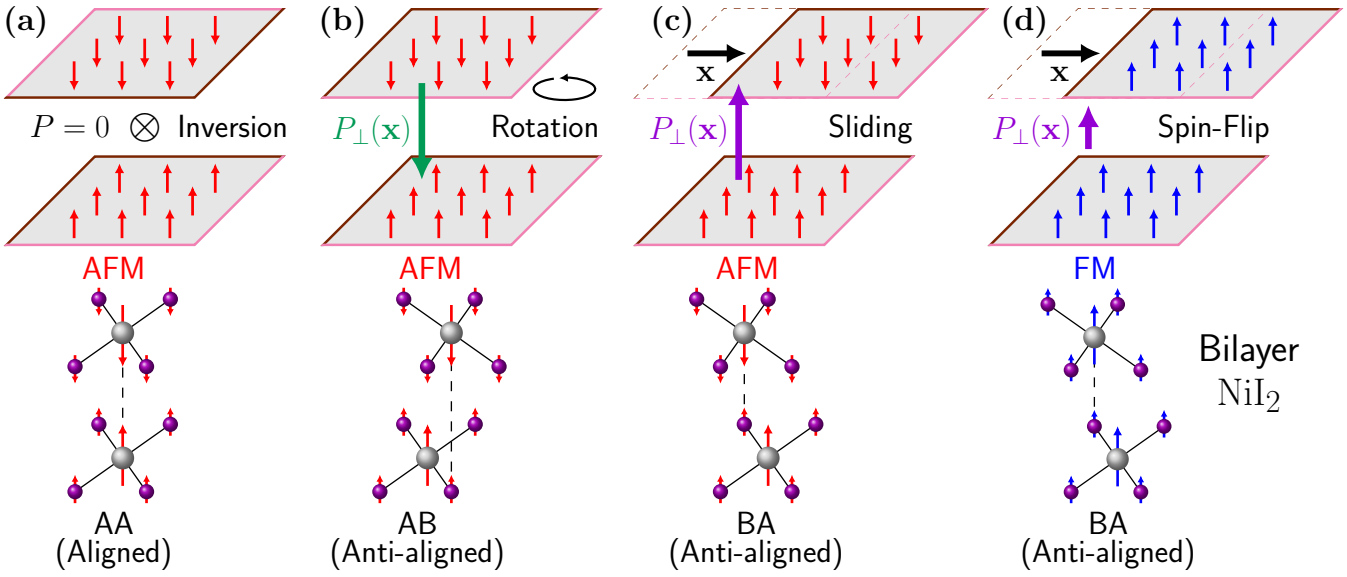

FIG. 1. Illustration of tuning multiferroic order and magnetoelectric coupling in vdW magnets with stacking engineering. **(a)** A vdW bilayer with an AFM interlayer spin configuration is sketched (spins denoted by red arrows), with color-coded edges to help identify the relative orientation of the layers. The bilayer has an inversion center and is nonpolar. **(b)** Rotating the layers by 180° breaks the inversion center, resulting in a stacking dependent polarization $P_\perp(\mathbf{x})$, denoted by the green (down) and purple (up) arrows. **(c)** A relative sliding $\mathbf{x}$ between the layers inverts the polarization. **(d)** Changing the interlayer spin order to FM (spins denoted by blue arrows) affects the magnitude of the polarization, but not the direction. The corresponding stackings in bilayer NiI_2 are illustrated below in each case. There is a relative shift between the layers along the unit cell diagonal: $\mathbf{x} = x(\mathbf{a}_1 + \mathbf{a}_2)$, where $x_{AA} = 0$, $x_{AB} = \frac{1}{3}$ and $x_{BA} = \frac{2}{3}$. Most of the magnetic moment is concentrated on the Ni atoms, with a small magnetic moment transferred to the I atoms.

field, and magnetization may be tuned using an electric field.

We propose a simple and general approach for engineering multiferroics with magnetoelectric coupling from vdW magnets through artificial stacking (see Fig. 1). This approach has already been successfully been applied to fabricate vdW ferroelectrics [11, 16, 18] mechanically using the tear and stack method. Using bilayer NiI_2 as an example, we show with *ab initio* calculations that by rotating one of the layers by 180° with respect to the natural bulk stacking, the bilayer becomes ferroelectric (see Fig. 2). Whether or not a system can be made ferroelectric can be determined simply from knowledge of the space groups of the different stackings [51]. It turns out that the symmetries of bilayers of NiI_2 and of TMDs in the H1 structure (such as MoS_2) are *exactly* the same upon rotation by 180° with respect to the natural bulk stacking (see Table I). This feature makes their ferroelectric properties identical.

Results.—We performed first-principles density functional theory (DFT) calculations to simulate the properties of bilayer NiI_2 [53]. We considered the aligned stacking which occurs naturally in bulk NiI_2, as well as the artificial anti-aligned stacking (see Fig. 1), with antiferromagnetic (AFM) and ferromagnetic (FM) interlayer spin configurations. We emphasize that throughout this work, AFM and FM always refer to the *interlayer* alignment of spins and not the alignment within a single layer. Because the wavelength of the spin spiral in NiI2 is relatively long (around 7 unit cells [49]), we consider uniform arrangements of spins pointing in the out-of-plane direction in each layer in order to avoid calculations involving large supercells.

Stacking	NiI_2		MoS_2	
	Aligned	Anti-aligned	Aligned	**Anti-aligned**
AA	$P\bar{3}m1$ (#164)	$P\bar{6}m2$ (#187)	$P\bar{6}m2$ (#187)	$P\bar{3}m1$ (#164)
AB	$P\bar{3}m1$ (#164)	$P3m1$ (#156)	$P3m1$ (#156)	$P\bar{3}m1$ (#164)
DW	$C2/m$ (#12)	$Abm2$ (#39)	$Abm2$ (#39)	$C2/m$ (#12)
BA	$P\bar{3}m1$ (#164)	$P3m1$ (#156)	$P3m1$ (#156)	$P\bar{3}m1$ (#164)

TABLE I. Space group analysis of the high-symmetry relative stackings in bilayer NiI2 and MoS_2. The bold font indicates the natural bulk stacking.

Fig. 2 shows the stacking energy $\mathcal{V}_{\text{stack}}$ and out-of-plane electronic dipole moment $p_\perp$ as a function of relative displacement x between the layers along the unit cell diagonal: $\mathbf{x} = x(\mathbf{a}_1 + \mathbf{a}_2)$ where $\mathbf{a}_i$ are the lattice vectors. Results for aligned and anti-aligned stackings as well as AFM (red) and FM (blue) interlayer spin configurations are shown [53]. The unit cell diagonal contains all of the high symmetry stacking configurations, namely AA ($x = 0, 1$), AB ($x = \frac{1}{3}$) and BA ($x = \frac{2}{3}$), and the domain wall (DW) stacking ($x = \frac{1}{2}$). The AFM configuration was found to be lower in energy

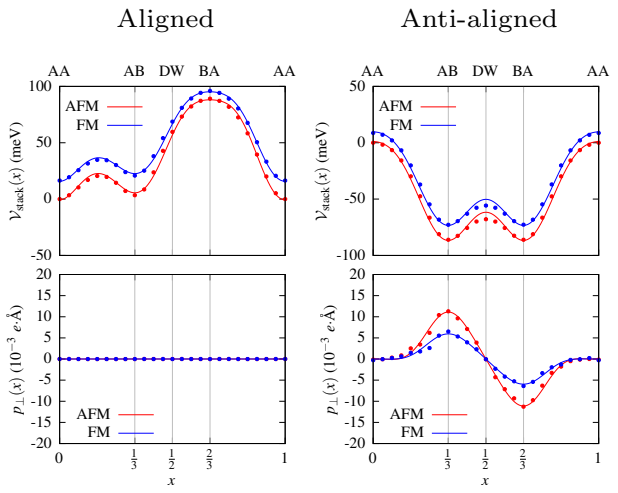

FIG. 2. Stacking energy $\mathcal{V}_{\text{stack}}$ and out-of-plane dipole moment $p_\perp$ for aligned and anti-aligned bilayer NiI2, as a function of relative stacking x along the unit cell diagonal. The labels AA, AB/BA and DW refer to the relative stackings, with AA (aligned) and AB/BA (ani-aligned) sketched in Fig. 1. Results for an AFM (FM) interlayer spin order are shown in red (blue). The dots show results from first-principles calculations and the solid lines show fits of the data to $\mathcal{C}_3$-symmetric basis functions, such as Eq. (1) for $p_\perp$.

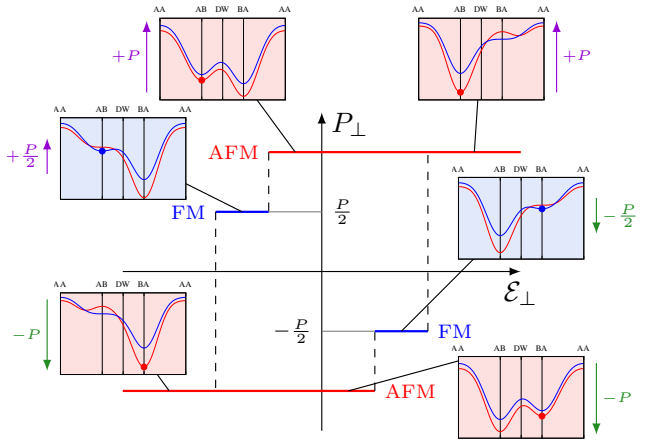

FIG. 3. Illustration of the ferroelectric hysteresis loop for anti-aligned bilayer NiI2. The free energies of the AFM (red) and FM (blue) interlayer spin configurations are sketched as a function of stacking, at six different points around the hysteresis loop. The dot shows the state that NiI_2 adopts for each electric field value, which is possibly metastable. The red (blue) background indicates that NiI_2 has an AFM (FM) interlayer spin order. The purple (green) arrows indicate that NiI_2 has polarization up (down). The jumps that decrease the magnitude of the polarization but do not change its sign are driven by a change in interlayer spin order (AFM $\rightarrow$ FM). The jumps which change the sign in polarization are driven by interlayer sliding (AB $\rightarrow$ BA) and are also accompanied by a change in interlayer spin order (FM $\rightarrow$ AFM).

for all stackings in both aligned and anti-aligned NiI_2. The aligned bilayer is non-polar for all stacking configurations as the inversion center between the layers is preserved upon sliding. For the anti-aligned stacking, the bilayer attains a stacking-dependent electronic dipole moment which is largest and of opposite sign for the energetically favorable AB and BA stackings, and is comparable to the dipole moments of other vdW ferroelectrics [53] which, while weak compared to conventional ferroelectrics such as oxide perovskites, can still be measured, switched, and can be used to dope proximal materials [10, 11, 16–22]. The polarization being an odd function of stacking and respecting the $\mathcal{C}_3$ rotation symmetry of the crystal takes the form [28]:

$$p_\perp(x,y) = p_1^{\text{odd}}\Big[\sin(2\pi x)+\sin(2\pi y)-\sin(2\pi(x+y))\Big]\,, \tag{1}$$

with $\mathbf{x}=(x,y)$ in fractional coordinates of the unit cell lattice constant. p_1^{odd} is a coefficient to be fit to DFT calculations. Additionally, anti-aligned NiI_2 also has a stacking-dependent *in-plane* polarization similar to rhombohedral hBN and TMDs [53].

Fig. 2 shows that the magnitude of the polarization in anti-aligned NiI_2 is sensitive to the interlayer spin configuration. Upon switching from AFM to FM the polarization decreases in magnitude by approximately a factor of 2. Fig. 3 illustrates the ferroelectric hysteresis loop in anti-aligned NiI_2 including the effects of this magnetoelectric coupling. In addition to the first-order interlayer sliding jumps in polarization there are also jumps in the magnitude of polarization, but not in sign, driven by a change in interlayer spin order. Thus, the spin order in anti-aligned NiI_2 can be switched using an applied electric field and the magnitude of the polarization can be tuned using a magnetic field. This can be explained by considering the free energy:

$$\mathcal{V}^\alpha(\mathbf{x},\mathcal{E}) = \mathcal{V}^\alpha_{\text{stack}}(\mathbf{x}) - \mathcal{E}\cdot p^\alpha(\mathbf{x})\,, \tag{2}$$

where $\alpha=$ AFM, FM, which is sketched in Fig. 3 at different points around the hysteresis loop. Applying an electric field $\mathcal{E}$ which is anti-aligned with the dipole moment (AB/BA), the FM configuration eventually becomes lower in energy. This results in a change in the interlayer spin order driven by a decrease in polarization. Increasing the electric field further, the other stacking configuration will eventually become preferable (BA/AB), resulting in polarization reversal through interlayer sliding.

The intralayer magnetic exchange parameters were obtained using the relativistic LKAG formalism [54] within a non-orthogonal localized basis framework, implemented in the GROGU code [53, 55]. The exchange and intra-atomic anisotropy tensors to any desired neighbor shell can be calculated, corresponding to the following Heisenberg Hamiltonian:

$$H_{\text{intra}} = \frac{1}{2}\sum_{i\neq j} J_\parallel^{ij}\,\mathbf{e}_i\cdot\mathbf{e}_j + \frac{1}{2}\sum_{i\neq j}\mathbf{e}_i J_{S,\parallel}^{ij}\,\mathbf{e}_j + \frac{1}{2}\sum_{i\neq j}\mathbf{D}^{ij}\cdot(\mathbf{e}_i\times\mathbf{e}_j)\,. \tag{3}$$

Here $\mathbf{e}_i$ is a unit vector pointing along the spin angular momentum of the localized magnetic entity placed at site i. $J_\parallel^{ij}$,

$J^{ij}_{S,\parallel}$ and $\mathbf{D}^{ij}$ are the isotropic exchange constants, symmetric traceless exchange tensor and Dzyaloshinskii-Moriya (DM) vectors between sites i and j, respectively. The interlayer isotropic exchange parameter $J_\perp$ was obtained from total energy differences between the FM and AFM bilayer spin alignments, mapped onto the effective Hamiltonian:

$$H_{\text{inter}} = J_\perp \mathbf{e}_1 \cdot \mathbf{e}_2 \,, \tag{4}$$

where $\mathbf{e}_1$ and $\mathbf{e}_2$ are unit vectors describing the spin directions in the first and second layers of bilayer NiI_2. The interlayer exchange changes by as much as a factor of 2 as a function of stacking [53] which suggests that the magnetic transition temperature is also stacking-dependent. The interlayer spin order does not change upon changing the stacking in contrast to other vdW magnets such as CrI_3 [38, 50, 56] and GdI_2 [52]: the AFM spin order is always energetically preferable at zero electric field.

By solving $\mathcal{V}^{\text{AFM}}(\mathbf{x}_{\text{AB}}, \mathcal{E}_c) = \mathcal{V}^{\text{FM}}(\mathbf{x}_{\text{AB}}, \mathcal{E}_c)$ for $\mathcal{E}_c$, the electric field required to change the interlayer spin order is $\mathcal{E}_c = 2.77$ V/Å for the AB/BA stackings in anti-aligned bilayer NiI_2. Similarly, the coercive magnetic field B_c required to switch from AFM to FM spin-order in anti-aligned NiI_2 and tune the electronic polarization is shown in Fig. 4 (a). B_c modulates with stacking, ranging between 25–40 T. In order to investigate the switching dynamics in more detail, we perform classical Monte Carlo (MC) calculations with a Heisenberg Hamiltonian to simulate anti-aligned bilayer NiI_2 in the AB stacking using a 64×64 supercell [53]. The intralayer magnetic interaction is frustrated due to the competition between the FM nearest neighbor (NN) exchange interactions and the AFM 3$^{\text{rd}}$ NN exchange interaction. The ground state from MC simulations is a spin spiral state with the in-plane spin and AFM interlayer ordering, as was found in Ref. [57]. By measuring the specific heat as a function of temperature, we find a Néel temperature of $T_N = 50$ K (Fig. 4 (b)). The average out-of-plane magnetization $M_\perp$ in response to an out-of-plane magnetic field $B_\perp$ is shown in Fig. 4 (c), for temperatures ranging from 0 K to 100 K. The magnetic field required to align the magnetic moment is $B_\perp \sim 800$ T at $T = 0$ K, and is reduced to about 200 T at finite temperature. In order to consider the magnetic field required to change the interlayer spin order, we calculate $\mathbf{e}_1 \cdot \mathbf{e}_2$, averaged over the supercell, as a function of magnetic field and temperature (Fig. 4 (d)): the interlayer spin order changes when $\mathbf{e}_1 \cdot \mathbf{e}_2$ changes sign. The coercive magnetic field required to change the interlayer spin order is also sensitive to temperature. Comparing Figs. 4 (c) and (d), the coercive field required to change the interlayer spin order is approximately half the field required to align all of the spins with the field (destroy the spin spiral state).

Discussion and conclusions.—We propose that vdW magnets can be made ferroelectric by fabricating multilayers in artificial stackings which break inversion symmetry, and we illustrate this concept using bilayer NiI_2 as an example. This approach can be generalized to other vdW magnets, although the resulting polar properties may differ depending on the crystal symmetries [58]. In addition, stacking-engineering

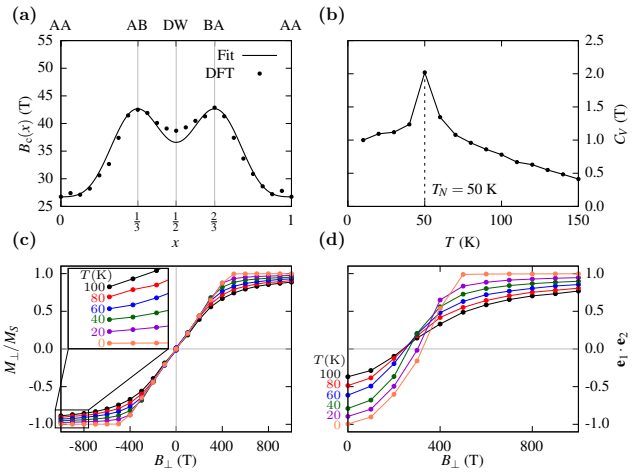

FIG. 4. **(a)** Estimate of the coercive magnetic field $B_c(x)$ in anti-aligned bilayer NiI_2. The points show the values of B_c obtained from DFT calculations at each stacking x. The solid line shows the values obtained from the fits to the stacking energies in Fig. 2. **(b)** Specific heat C_V of the system as a function of temperature T from MC simulations. C_V is normalized such that $C_V(T \to 0) = 1$. The peak at 50 K indicates the Néel temperature T_N. **(c)** Average out-of-plane magnetization $M_\perp$, in units of the spontaneous magnetization M_S as a function of perpendicular magnetic field $B_\perp$ and temperature T. **(d)** Average interlayer spin order $\mathbf{e}_1 \cdot \mathbf{e}_2$ as a function of perpendicular magnetic field $B_\perp$ and temperature T.

also results in a novel strong magnetoelectric coupling in vdW magnets without centrosymmetry. The magnetoelectric coupling occurs between interfacial polarization arising from interlayer charge transfer and the interlayer spin order in the bilayer: changes in the electronic structure induced by changes in the interlayer spin ordering modify the electronic polarization. As a case in point, we find a new type of multiferroic order in bilayer NiI_2 upon rotation of the layers to the anti-aligned stacking. We predict additional jumps in the ferroelectric hysteresis loop, with the polarization changing in magnitude by a factor of two as a result of changes in the interlayer spin order. While we expect the magnetoelectric coupling to be general to vdW magnets, determined only by symmetry, the existence of the additional jumps in the hysteresis loop (Fig. 3) is determined by the relative sizes of the energy barriers separating the polar stackings, and the AFM/FM interlayer spin orders, which may be material dependent. Additionally, this balance may be sensitive to the switching mechanisms, as discussed below.

The coercive fields required to achieve this switching are predicted to be unrealistically large by our calculations, with electric fields of order 1 V/Å and magnetic fields of order 10–100 T (similar values were predicted in Ref. [57]). We note that the large coercive fields obtained in DFT/MC calculations correspond to the physical mechanism of polarization/magnetization reversal. Experimentally however, switching occurs due to nano-domain nucleation and subsequent growth due to domain wall propagation. This switching mech-

anism needs to overcome much lower energy barriers and therefore requires much smaller coercive fields, typically below $\mathcal{E} = 0.2$ V/nm for vdW ferroelectrics [11, 16, 18] and $B = 1$ T for vdW magnets [7, 59, 60].

We expect that our predictions of coupled multiferroic order (Fig. 3) may be validated using similar experimental techniques used to characterize vdW ferroelectrics and magnets. Techniques to measure ferroelectric hysteresis in rhombohedral hBN [11, 21] and TMDs [22] may be used to detect additional jumps in polarization induced by spin flips. The polarization in NiI_2 can be probed through bulk photovoltaic effect (BPVE) measurements, which can also provide information on the role of domain walls in switching [45]. Additionally, polar domains can be imaged using piezoresponse force microscopy (PFM) measurements [10], which can be done under a magnetic field [61], or transmission electron microscopy (TEM) measurements [18]. For ultrathin multiferroics, magneto-optical measurements such as circular dichroism (CD) and magneto-optical Kerr effect (MOKE) can be used to determine the magnetization as well as probe magnetic textures [45].

In the present work we considered the interplay between electronic polarization and interlayer spin order assuming homogeneous spin textures within each layer. The coupling between polarization and complex spin textures may lead to more interesting and exotic multiferroic coupling. For example, suppose the spin spirals in both layers are offset from one another, which can be described by a relative phase shift. If the relative phase shift is the 0 (π), the interlayer spin order is FM (AFM). By using an electric field to switch the polarization through interlayer sliding, the relative phase between the two spin spirals and hence the interlayer spin order may also change.

Finally, we propose that stacking vdW magnets to form moiré superlattices may be a route to engineering multiferroic topological structures, in which polar and spin topologies are coupled and may both be controlled with magnetic and electric fields. Considering the out-of-plane and in-plane polarization in anti-aligned bilayer NiI_2, a twist by a small angle about the 180° orientation will result in a regular network of polar merons and antimerons (winding numbers $Q \pm \frac{1}{2}$ in each domain) [29, 53]. Additionally, it is known that magnetic skyrmions can spontaneously form in NiI_2 in the few-layer limit [57]. By precisely engineering a moiré superlattice of period commensurate with the magnetic skyrmion wavelength, one may achieve the coexistence and coupling of polar and magnetic topological structures in a single device.

Acknowledgements.—D.B. and E.K. acknowledge the US Army Research Office (ARO) MURI project under grant No. W911NF-21-0147 and the Simons Foundation award No. 896626. G.M.-C. and J.F. have been funded by MCIN/AEI/10.13039/501100011033/FEDER, UE via project PID2022-137078NB-100 and by Asturias FICYT under grant AYUD/2021/51185 with the support of FEDER funds. G.M.-C. has been supported by Programa "Severo Ochoa" de Ayudas para la investigación y docencia del Principado de Asturias. X.H. and Ph.G. acknowledge financial support from F.R.S.-FNRS Belgium through the PDR project PROMOSPAN (Grant No. T.0107.20). R.C. acknowledges support by the Department of Energy, Office of Science, Office of Basic Energy Sciences, under Award No. DE-SC0019126. J.F. acknowledges a discussion with A. Hierro on the role of magnetization reversal versus domain growth in experimental magnetic materials.

[1] K. S. Novoselov, A. Mishchenko, A. Carvalho, and A. Castro Neto, Science **353**, aac9439 (2016).
[2] A. K. Geim and I. V. Grigorieva, Nature **499**, 419 (2013).
[3] M. Gibertini, M. Koperski, A. F. Morpurgo, and K. S. Novoselov, Nat. Nanotechnol. **14**, 408 (2019).
[4] K. Khan, A. K. Tareen, M. Aslam, R. Wang, Y. Zhang, A. Mahmood, Z. Ouyang, H. Zhang, and Z. Guo, J. Mater. Chem. C **8**, 387 (2020).
[5] N. R. Glavin, R. Rao, V. Varshney, E. Bianco, A. Apte, A. Roy, E. Ringe, and P. M. Ajayan, Adv. Mater. **32**, 1904302 (2020).
[6] P. Kumbhakar, J. S. Jayan, A. S. Madhavikutty, P. Sreeram, S. Appukuttan, T. Ito, and C. S. Tiwary, IScience (2023).
[7] B. Huang, G. Clark, E. Navarro-Moratalla, D. R. Klein, R. Cheng, K. L. Seyler, D. Zhong, E. Schmidgall, M. A. McGuire, D. H. Cobden, *et al.*, Nature **546**, 270 (2017).
[8] C. Gong, L. Li, Z. Li, H. Ji, A. Stern, Y. Xia, T. Cao, W. Bao, C. Wang, Y. Wang, *et al.*, Nature **546**, 265 (2017).
[9] L. Li and M. Wu, ACS Nano **11**, 6382 (2017).
[10] M. V. Stern, Y. Waschitz, W. Cao, I. Nevo, K. Watanabe, T. Taniguchi, E. Sela, M. Urbakh, O. Hod, and M. B. Shalom, Science **372**, 1462 (2021).
[11] K. Yasuda, X. Wang, K. Watanabe, T. Taniguchi, and P. Jarillo-Herrero, Science **372**, 1458 (2021).
[12] N. D. Mermin and H. Wagner, Phys. Rev. Lett. **17**, 1133 (1966).
[13] Šiškins, Makars and Kurdi, Samer and Lee, Martin and Slotboom, Benjamin JM and Xing, Wenyu and Mañas-Valero, Samuel and Coronado, Eugenio and Jia, Shuang and Han, Wei and van der Sar, Toeno and others, npj 2D Mater. Appl. **6**, 41 (2022).
[14] H. Y. Lv, W. J. Lu, X. Luo, X. B. Zhu, and Y. P. Sun, Phys. Rev. B **99**, 134416 (2019).
[15] G. Martínez-Carracedo, L. Oroszlány, A. García-Fuente, L. Szunyogh, and J. Ferrer, Phys. Rev. B **107**, 035432 (2023).
[16] X. Wang, K. Yasuda, Y. Zhang, S. Liu, K. Watanabe, T. Taniguchi, J. Hone, L. Fu, and P. Jarillo-Herrero, Nat. Nanotechnol. **17**, 367 (2022).
[17] A. Weston, E. G. Castanon, V. Enaldiev, F. Ferreira, S. Bhattacharjee, S. Xu, H. Corte-León, Z. Wu, N. Clark, A. Summerfield, *et al.*, Nat. Nanotechnol. **17**, 390 (2022).
[18] K. Ko, A. Yuk, R. Engelke, S. Carr, J. Kim, D. Park, H. Heo, H.-M. Kim, S.-G. Kim, H. Kim, *et al.*, Nat. Mater. , 1 (2023).
[19] L. Molino, L. Aggarwal, V. Enaldiev, R. Plumadore, V. I. Fal´ ko, and A. Luican-Mayer, Adv. Mater. **35**, 2207816 (2023).
[20] M. Van Winkle, N. Dowlatshahi, N. Khaloo, M. Iyer, I. M. Craig, R. Dhall, T. Taniguchi, K. Watanabe, and D. K. Bediako, Nat. Nanotechnol. , 1 (2024).
[21] K. Yasuda, E. Zalys-Geller, X. Wang, D. Bennett, S. S. Cheema, K. Watanabe, T. Taniguchi, E. Kaxiras, P. Jarillo-Herrero, and R. Ashoori, Science , eadp3575 (2024).

[22] R. Bian, R. He, E. Pan, Z. Li, G. Cao, P. Meng, J. Chen, Q. Liu, Z. Zhong, W. Li, *et al.*, Science , eado1744 (2024).
[23] R. Bistritzer and A. H. MacDonald, PNAS **108**, 12233 (2011).
[24] Y. Cao, V. Fatemi, S. Fang, K. Watanabe, T. Taniguchi, E. Kaxiras, and P. Jarillo-Herrero, Nature **556**, 43 (2018).
[25] Y. Cao, V. Fatemi, A. Demir, S. Fang, S. L. Tomarken, J. Y. Luo, J. D. Sanchez-Yamagishi, K. Watanabe, T. Taniguchi, E. Kaxiras, *et al.*, Nature **556**, 80 (2018).
[26] D. Bennett, D. T. Larson, L. Sharma, S. Carr, and E. Kaxiras, Phys. Rev. B **109**, 155422 (2024).
[27] D. Bennett and B. Remez, npj 2D Mater. Appl. **6**, 1 (2022).
[28] D. Bennett, Phys. Rev. B **105**, 235445 (2022).
[29] D. Bennett, G. Chaudhary, R.-J. Slager, E. Bousquet, and P. Ghosez, Nat. Commun. **14**, 1629 (2023).
[30] D. Bennett, W. J. Jankowski, G. Chaudhary, E. Kaxiras, and R.-J. Slager, Phys. Rev. Res. **5**, 033216 (2023).
[31] W. J. Jankowski, D. Bennett, A. Agarwal, G. Chaudhary, and R.-J. Slager, arXiv:2404.16919 (2024).
[32] T.-H.-Y. Vu, D. Bennett, G. N. Pallewella, M. H. Uddin, K. Xing, W. Zhao, S. H. Lee, Z. Mao, J. B. Muir, L. Jia, J. A. Davis, K. Watanabe, T. Taniguchi, S. Adam, P. Sharma, M. S. Fuhrer, and M. T. Edmonds, arxiv:2405.15126 (2024).
[33] S. Das, Y. Tang, Z. Hong, M. Gonçalves, M. McCarter, C. Klewe, K. Nguyen, F. Gómez-Ortiz, P. Shafer, E. Arenholz, *et al.*, Nature **568**, 368 (2019).
[34] L. Han, C. Addiego, S. Prokhorenko, M. Wang, H. Fu, Y. Nahas, X. Yan, S. Cai, T. Wei, Y. Fang, *et al.*, Nature **603**, 63 (2022).
[35] J. Junquera, Y. Nahas, S. Prokhorenko, L. Bellaiche, J. Íñiguez, D. G. Schlom, L.-Q. Chen, S. Salahuddin, D. A. Muller, L. W. Martin, and R. Ramesh, Rev. Mod. Phys. **95**, 025001 (2023).
[36] G. Sánchez-Santolino, V. Rouco, S. Puebla, H. Aramberri, V. Zamora, M. Cabero, F. Cuellar, C. Munuera, F. Mompean, M. Garcia-Hernandez, *et al.*, Nature **626**, 529 (2024).
[37] T. Song, Q.-C. Sun, E. Anderson, C. Wang, J. Qian, T. Taniguchi, K. Watanabe, M. A. McGuire, R. Stöhr, D. Xiao, *et al.*, Science **374**, 1140 (2021).
[38] A. O. Fumega and J. L. Lado, 2D Mater. **10**, 025026 (2023).
[39] N. A. Spaldin and M. Fiebig, Science **309**, 391 (2005).
[40] N. A. Spaldin and R. Ramesh, Nat. Mater. **18**, 203 (2019).
[41] J. Wang, J. Neaton, H. Zheng, V. Nagarajan, S. Ogale, B. Liu, D. Viehland, V. Vaithyanathan, D. Schlom, U. Waghmare, *et al.*, Science **299**, 1719 (2003).
[42] H. Liu, X. Wang, J. Wu, Y. Chen, J. Wan, R. Wen, J. Yang, Y. Liu, Z. Song, and L. Xie, ACS nano **14**, 10544 (2020).
[43] H. Ju, Y. Lee, K.-T. Kim, I. H. Choi, C. J. Roh, S. Son, P. Park, J. H. Kim, T. S. Jung, J. H. Kim, *et al.*, Nano Lett. **21**, 5126 (2021).
[44] S. Jenkins, L. Rozsa, U. Atxitia, R. L. F. Evans, K. S. Novoselov, and E. J. G. Santos, Nat. Commun. **13**, 6917 (2022).
[45] Q. Song, C. A. Occhialini, E. Ergeçen, B. Ilyas, D. Amoroso, P. Barone, J. Kapeghian, K. Watanabe, T. Taniguchi, A. S. Botana, *et al.*, Nature **602**, 601 (2022).
[46] M. Mostovoy, Phys. Rev. Lett. **96**, 067601 (2006).
[47] H. J. Xiang, E. J. Kan, Y. Zhang, M.-H. Whangbo, and X. G. Gong, Phys. Rev. Lett. **107**, 157202 (2011).
[48] P. C. Hohenberg and A. P. Krekhov, Phys. Rep. **572**, 1 (2015).
[49] A. O. Fumega and J. Lado, 2D Mater. **9**, 025010 (2022).
[50] N. Sivadas, S. Okamoto, X. Xu, C. J. Fennie, and D. Xiao, Nano Lett. **18**, 7658 (2018).
[51] J. Ji, G. Yu, C. Xu, and H. J. Xiang, Phys. Rev. Lett. **130**, 146801 (2023).
[52] W. Xun, C. Wu, H. Sun, W. Zhang, Y.-Z. Wu, and P. Li, Nano Lett. **24**, 3541 (2024).
[53] See Supplemental Material [url] for details of first-principles calculations and additional results, which includes Refs. [62–72].
[54] A. I. Liechtenstein, M. Katsnelson, V. Antropov, and V. Gubanov, J. Magn. Magn. Mater. **67**, 65 (1987).
[55] G. Martínez-Carracedo, L. Oroszlány, A. García-Fuente, B. Nyári, L. Udvardi, L. Szunyogh, and J. Ferrer, Phys. Rev. B **108**, 214418 (2023).
[56] W. Sun, W. Wang, R. Hu, C. Yang, L. Li, S. Huang, X. Li, and Z. Cheng, ACS Appl. Nano Mater. **6**, 17021 (2023).
[57] D. Amoroso, P. Barone, and S. Picozzi, Nat. Commun. **11**, 5784 (2020).
[58] S. P. Poudel, J. M. Marmolejo-Tejada, J. E. Roll, M. A. Mosquera, and S. Barraza-Lopez, Phys. Rev. B **107**, 195128 (2023).
[59] Y. Wen, Z. Liu, Y. Zhang, C. Xia, B. Zhai, X. Zhang, G. Zhai, C. Shen, P. He, R. Cheng, *et al.*, Nano Lett. **20**, 3130 (2020).
[60] Z. Fei, B. Huang, P. Malinowski, W. Wang, T. Song, J. Sanchez, W. Yao, D. Xiao, X. Zhu, A. F. May, *et al.*, Nat. Mater. **17**, 778 (2018).
[61] L. Keeney, T. Maity, M. Schmidt, A. Amann, N. Deepak, N. Petkov, S. Roy, M. E. Pemble, and R. W. Whatmore, J. Am. Ceram. Soc. **96**, 2339 (2013).
[62] J. M. Soler, E. Artacho, J. D. Gale, A. García, J. Junquera, P. Ordejón, and D. Sánchez-Portal, J. Phys. Condens. Matter **14**, 2745 (2002).
[63] D. Hamann, Phys. Rev. B **88**, 085117 (2013).
[64] A. García, M. J. Verstraete, Y. Pouillon, and J. Junquera, Comput. Phys. Commun. **227**, 51 (2018).
[65] M. Van Setten, M. Giantomassi, E. Bousquet, M. J. Verstraete, D. R. Hamann, X. Gonze, and G.-M. Rignanese, Comput. Phys. Commun. **226**, 39 (2018).
[66] N. R. Papior, G. Calogero, and M. Brandbyge, J. Phys.: Condens. Matter **30**, 25LT01 (2018).
[67] X. Gonze, B. Amadon, P.-M. Anglade, J.-M. Beuken, F. Bottin, P. Boulanger, F. Bruneval, D. Caliste, R. Caracas, M. Côté, *et al.*, Comput. Phys. Commun. **180**, 2582 (2009).
[68] H. J. Monkhorst and J. D. Pack, Phys. Rev. B **13**, 5188 (1976).
[69] J. P. Perdew, K. Burke, and M. Ernzerhof, Phys. Rev. Lett. **77**, 3865 (1996).
[70] S. Grimme, J. Antony, S. Ehrlich, and H. Krieg, J. Chem. Phys. **132** (2010).
[71] J. Neugebauer and M. Scheffler, Phys. Rev. B **46**, 16067 (1992).
[72] M. J. Rutter, Comput. Phys. Commun. **225**, 174 (2018).

SUPPLEMENTARY MATERIAL
Stacking-engineered ferroelectricty and multiferroic order in van der Waals magnets

Daniel Bennett,[1,*] Gabriel Martínez-Carracedo,[2,3] Xu He,[4] Jaime Ferrer,[2,3] Philippe Ghosez,[4] Riccardo Comin,[5] and Efthimios Kaxiras[1,6]

[1]*John A. Paulson School of Engineering and Applied Sciences, Harvard University, Cambridge, Massachusetts 02138, USA*
[2]*Departamento de Física, Universidad de Oviedo, 33007 Oviedo, Spain*
[3]*Centro de Investigación en Nanomateriales y Nanotecnología, Universidad de Oviedo-CSIC, 33940 El Entrego, Spain*
[4]*Theoretical Materials Physics, Q-MAT, University of Liège, B-4000 Sart Tilman, Belgium*
[5]*Department of Physics, Massachusetts Institute of Technology, Cambridge, MA, USA*
[6]*Department of Physics, Harvard University, Cambridge, Massachusetts 02138, USA*

FIRST-PRINCIPLES CALCULATIONS

First-principles density functional theory (DFT) calculations were performed using the SIESTA [1] code, version 5.0, with norm-conserving [2] PSML pseudopotentials [3], obtained from Pseudo-Dojo [4]. A basis of triple-ζ double polarized (TZDP) orbitals were used for all calculations, the cutoff radii of which were determined with an energy shift of 20 meV. Diffuse orbitals [5] were added ($5s$ and $5p$ for Ni, $6s$ and $6p$ for I) in order to better treat the interlayer interactions and the decay of the charge density into the vacuum region. We employed cutoff radii of 15 bohr for all diffuse orbitals, which were found to yield electronic band structures in good agreement with results obtained from the ABINIT plane-wave code [6] using the same PSML pseudopotentials. A Monkhorst-Pack **k**-point grid [7] of 18×18 was used in all calculations and, the real space grid was determined with an energy cutoff of 1000 Ry. We use the PBE exchange-correlation functional [8] in all calculations. A DFT-D3 dispersion correction [9] was included in order to treat the long range interactions between the layers, with a dipole correction in the vacuum region to prevent dipole-dipole interactions between periodic images [10].

A Hubbard-U correction was included on the Ni $3d$ orbitals with a value of $U = 1.8$ eV, following Ref. [11], where the value of U and its effect on the magnetic ordering in nickel halide layers was carefully tested: it was found that the magnetic exchange parameters are qualitatively unaffected by the value of U in the range 1–3 eV. SOC was included in all calculations except for geometry relaxation of the interlayer separation in the bilayers. The initial spin configuration was taken to be $\pm 2\mu_B$ in the out-of-plane direction on the Ni atoms of each layer, the opposite (same) sign for AFM (FM) interlayer spin configurations. The spins did not deviate much from the initial configuration after convergence of the calculations, except for a small transfer of some spin to the I atoms.

A lattice constant of 4.00 Å was obtained for monolayer NiI_2, in good agreement with the experimentally reported value of 3.98 Å, which was used in the bilayer calculations. Geometry relaxations were then performed (without SOC) in order to determine the interlayer separation, using a force tolerance of 0.1 meV/Å. The top layer was translated above the bottom layer along the unit cell diagonal, for both aligned and anti-aligned stacking configurations, and for both AFM and FM interlayer spin configurations. After relaxation, calculations were then repeated including SOC. The polarization was calculated from Berry phases.

Because the volume, and hence the polarization, is ill-defined in 2D materials, we plot the dipole moment in the main text. In order to better compare with conventional ferroelectrics, we plot the stacking-dependent polarization in Fig. S1. Here, the volume of the bilayer is defined to be the in-plane area of the unit cell times the interlayer separation, which is taken to be the vertical separation between the Ni atoms in each layer.

* dbennett@seas.harvard.edu

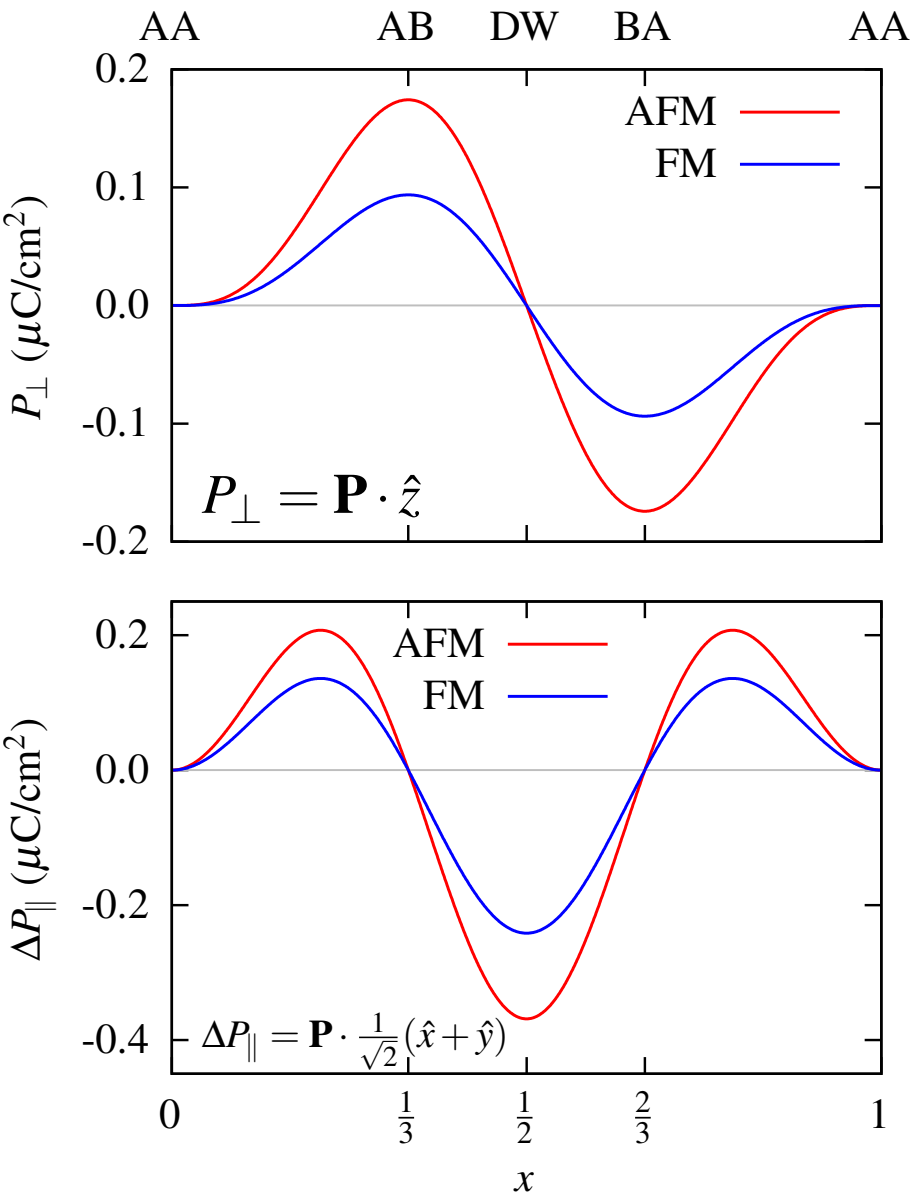

FIG. S1. Plot of the out-of-plane (top) and in-plane (bottom) polarization as a function of stacking in anti-aligned bilayer NiI_2, for AFM (red) and FM (blue) interlayer spin configurations.

DIFFERENTIAL CHARGE DENSITY

Fig. S2 shows the differential electronic charge density of anti-aligned NiI_2 for the AB and BA stackings, obtained using the C2X utility [12]. We can see that the direction of the transferred charge switches upon changing the stacking configurations. Upon changing the interlayer spin order, a small difference in the differential charge density is observed.

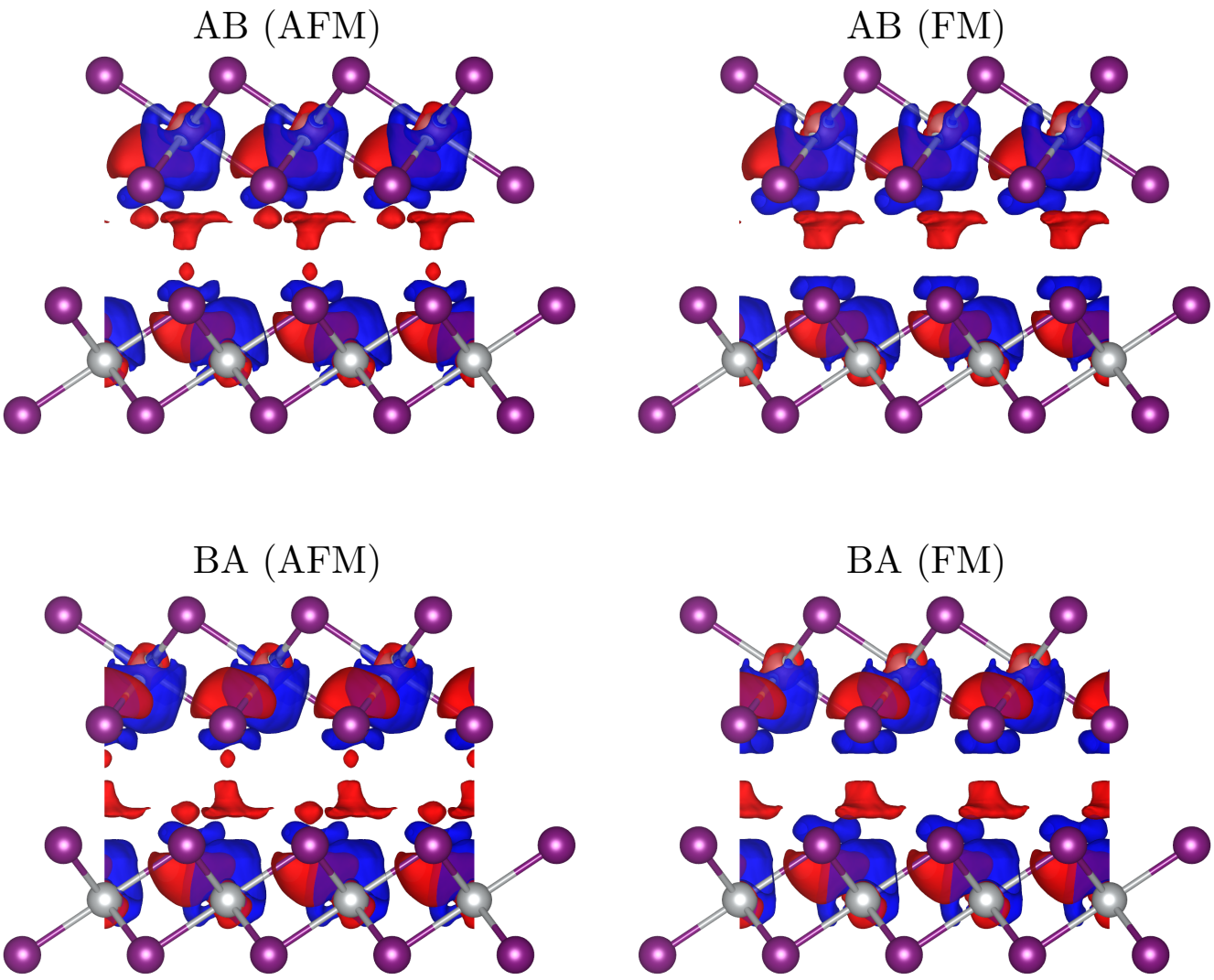

FIG. S2. Differential charge densities for the AB/BA stackings and AFM/FM interlayer spin configurations, obtained by subtracting the total real-space charge densities of the individual monolayers from the total density of the bilayer in each case. The blue and red isosurfaces correspond to negative and positive charge, respectively.

ORBITAL-PROJECTED BAND STRUCTURES

Fig. S3 shows the orbital-projected electronic band structures of AB stacked anti-aligned NiI_2 for the AFM and FM interlayer spin configurations. The valence bands and top two conduction bands mainly consist of strong hybridization between the Ni $3d$ states and the I $5p$ states, and the higher conduction bands are mainly described by the Ni $4s$ states. Changing from the AFM to the FM spin order results in small splittings in the bands due to the breaking of time reversal symmetry. Although the general orbital character of the bands remains the same upon changing the spin order, these small changes in the electronic structure result in a change in electronic polarization. While the changes are small, the electronic charge transfer is weak, and small changes in the electronic structure are sufficient to cause a large relative change in polarization, by a factor of ~ 2.

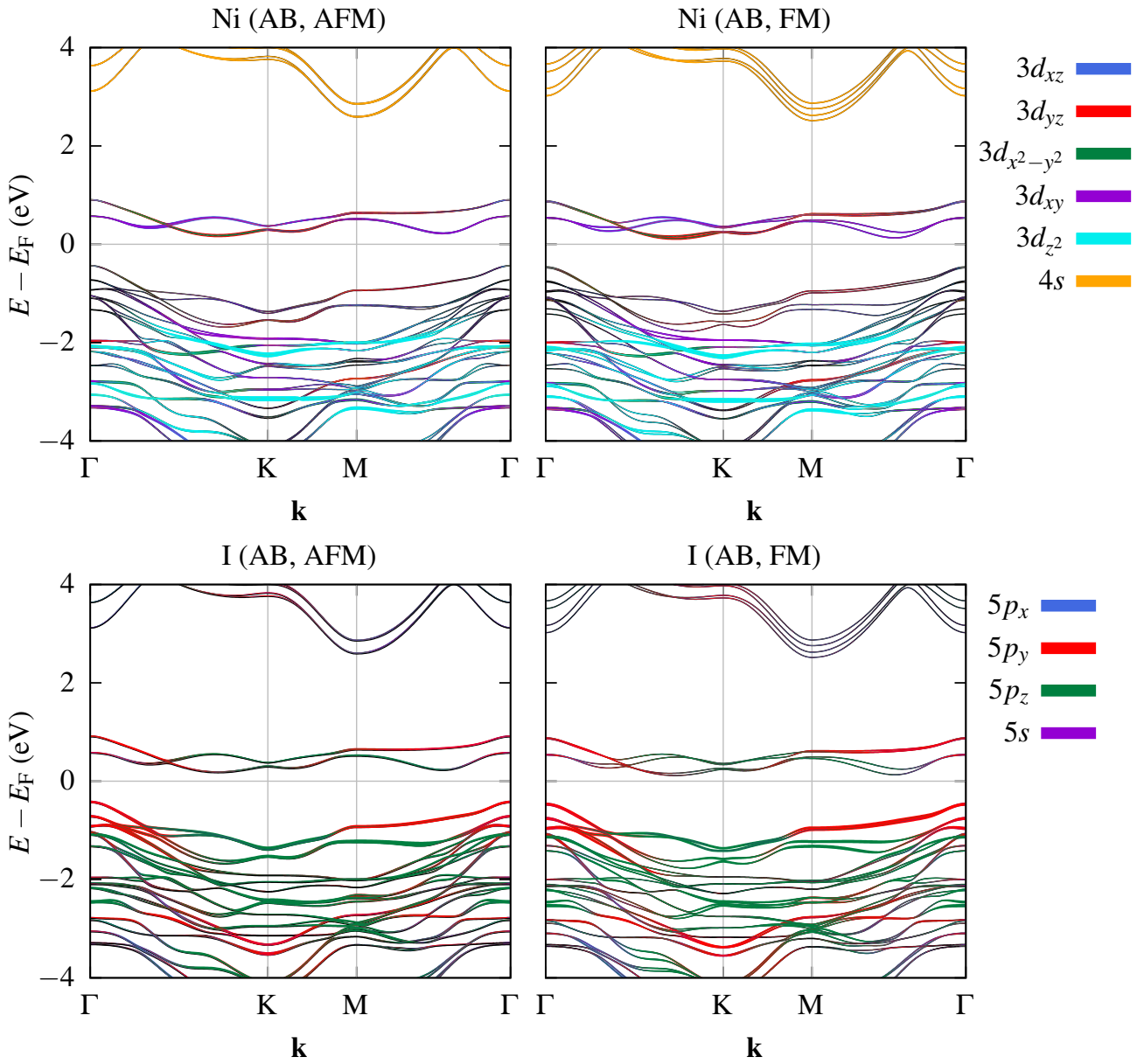

FIG. S3. Orbital-projected band structures for anti-aligned bilayer NiI2 for the AB stacking, and for AFM (left) and FM (right) interlayer spin configurations. Projections onto Ni (top) and I (bottom) orbitals are shown separately.

TOPOLOGICAL POLARIZATION

The total polarization, including both in-plane and out-of-plane components and the winding of the polarization are shown as a function of stacking in Fig. S4 for AFM and FM anti-aligned bilayer NiI_2.

The winding of the polarization field (topological charge) was calculated following the methodology in Ref. [13]. The total winding number is given by

$$Q = \frac{1}{4\pi} \int \mathbf{P} \cdot (\partial_x \mathbf{P} \times \partial_y \mathbf{P}) \, \mathrm{d}\mathbf{x} \,, \tag{S1}$$

where $\mathbf{P}$ is normalized and $\mathbf{x} = (x, y)$. The polarization in the unit cell is discretized on a fine grid with spacing Δ, and a plaquette is constructed around each grid point. The plaquettes form a grid which is offset from the original by half a grid spacing, which avoids the nonpolar AA stacking. The local winding or topological charge can then be defined as

$$q(\mathbf{x}) = \frac{1}{4\pi} \left(A(P_1, P_2, P_3) + A(P_1, P_3, P_4) \right) \,, \tag{S2}$$

where A is the signed area spanned by three points on a sphere:

$$\begin{aligned} A(P_1, P_2, P_3) = 2 \arg\big(1 + P_1 \cdot P_2 + P_2 \cdot P_3 + P_3 \cdot P_1 \\ + i P_1 \cdot (P_2 \times P_3)\big) \end{aligned} \,. \tag{S3}$$

$q(\mathbf{x})$ is shown in Figs. S4 (c) and (f) for AFM and FM anti-aligned bilayer NiI_2, respectively. The total charge is then given by

$$Q = \sum_{\mathbf{x}} q(\mathbf{x}) \,. \tag{S4}$$

The winding numbers of AB and BA domains converge to $Q_{\mathrm{AB}} = -Q_{\mathrm{BA}} = \frac{1}{2}$ with grid spacing Δ.

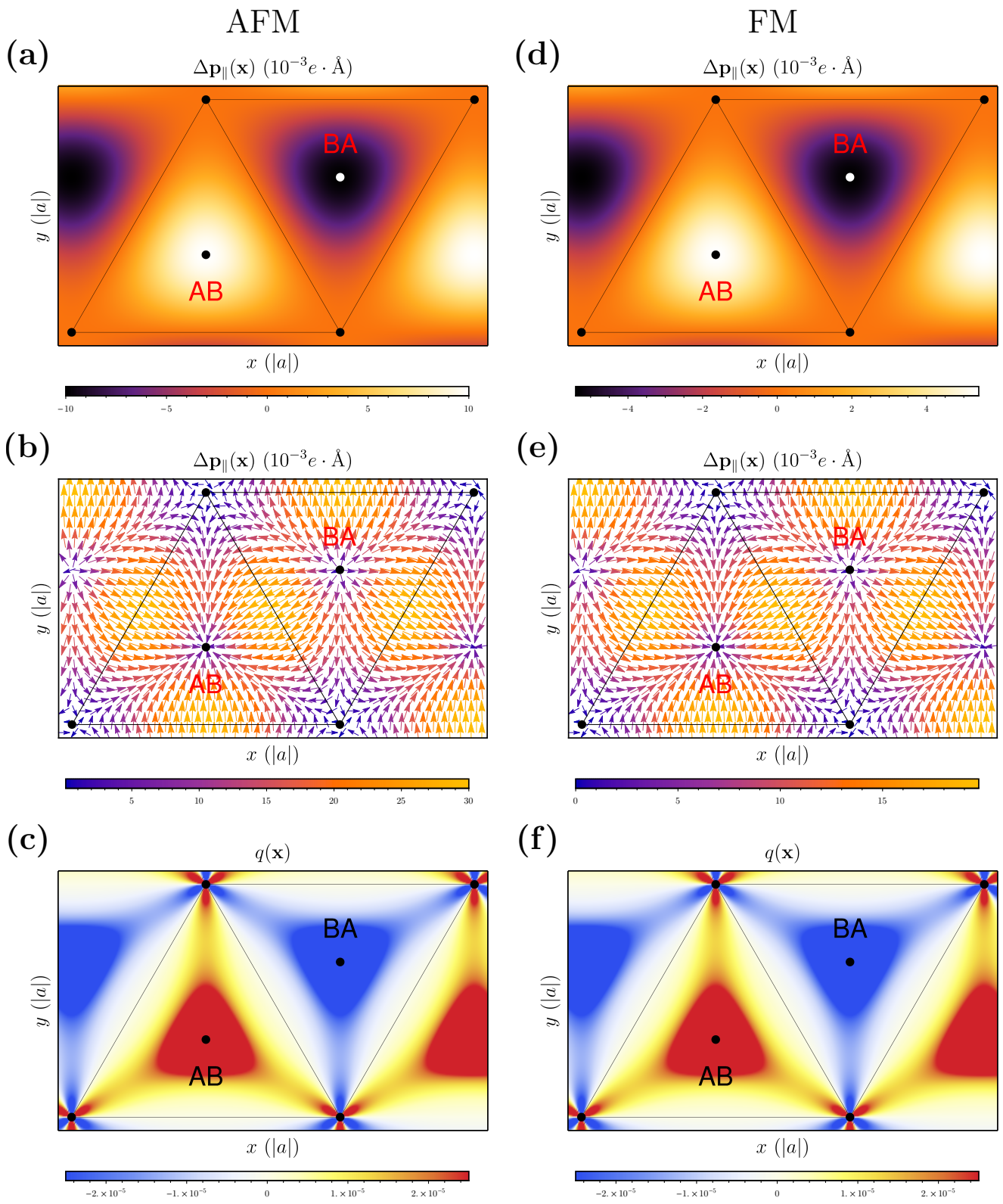

FIG. S4. **(a)**–**(c)** Polarization in the **(a)** out-of-plane and **(b)** in-plane directions, and **(c)** winding of the total polarization, as a function of relative stacking in AFM anti-aligned bilayer NiI_2. **(d)**–**(f)** Polarization in the **(d)** out-of-plane and **(e)** in-plane directions, and **(f)** winding of the total polarization, as a function of relative stacking in FM anti-aligned bilayer NiI_2.

MAGNETIC EXCHANGE PARAMETERS

The GROGU code [14] was used to calculate the intralayer magnetic exchange parameters of the Heisenberg Hamiltonian in Eq. 3 in the main text. As the dominant DM interaction is given by first nearest neighbors and the radial component is negligible, it is convenient to express DM vectors in cylindrical coordinates $\mathbf{D}^{ij} = (D^r, D^\theta, D^z)$ where the radial component points along the bond.

GROGU calculations were performed using a dense Monkhorst-Pack grid of 100×100 which take a self-consistent Hamiltonian obtained from SIESTA calculations (including SOC). The localized magnetic entities were projected onto $3d$-orbitals of the Ni atoms.

Fig. S5 shows the exchange parameters between the Ni atoms in bilayer NiI_2 as a function of stacking. The intralayer parameters $J_\parallel$ were calculated using the LKAG method [15], which are slightly modulated as a function of stacking. The interlayer exchange parameters $J_\perp$ are governed by long-range electrostatic interactions, meaning that they are very sensitive to many computational parameters. We therefore estimate them from the total energy differences between the AFM and FM interlayer spin configurations at each stacking. A more detailed treatment of the interlayer exchange interactions in vdW magnets using the LKAG method is left for a subject of future research. The nearest neighbor (NN) intralayer interactions are underestimated when compared to the value obtained in Ref. [11], which uses the supercell method. This is due to the strong hybridization between the Ni and I atoms in each layer, which carry much of the exchange. However, the LKAG method allows us to calculate exchanges between an arbitrary number of NNs using a single unit cell, and study the stacking dependence of the magnetic properties. The interlayer exchange changes by as much as a factor of 2 as a function of stacking. The interlayer spin order however, does not change upon changing the stacking, in contrast to e.g. CrI_3 [16], and the AFM spin order is always energetically preferable at zero electric field. Because inversion symmetry is broken, the DM vectors are non-zero in the bilayer.

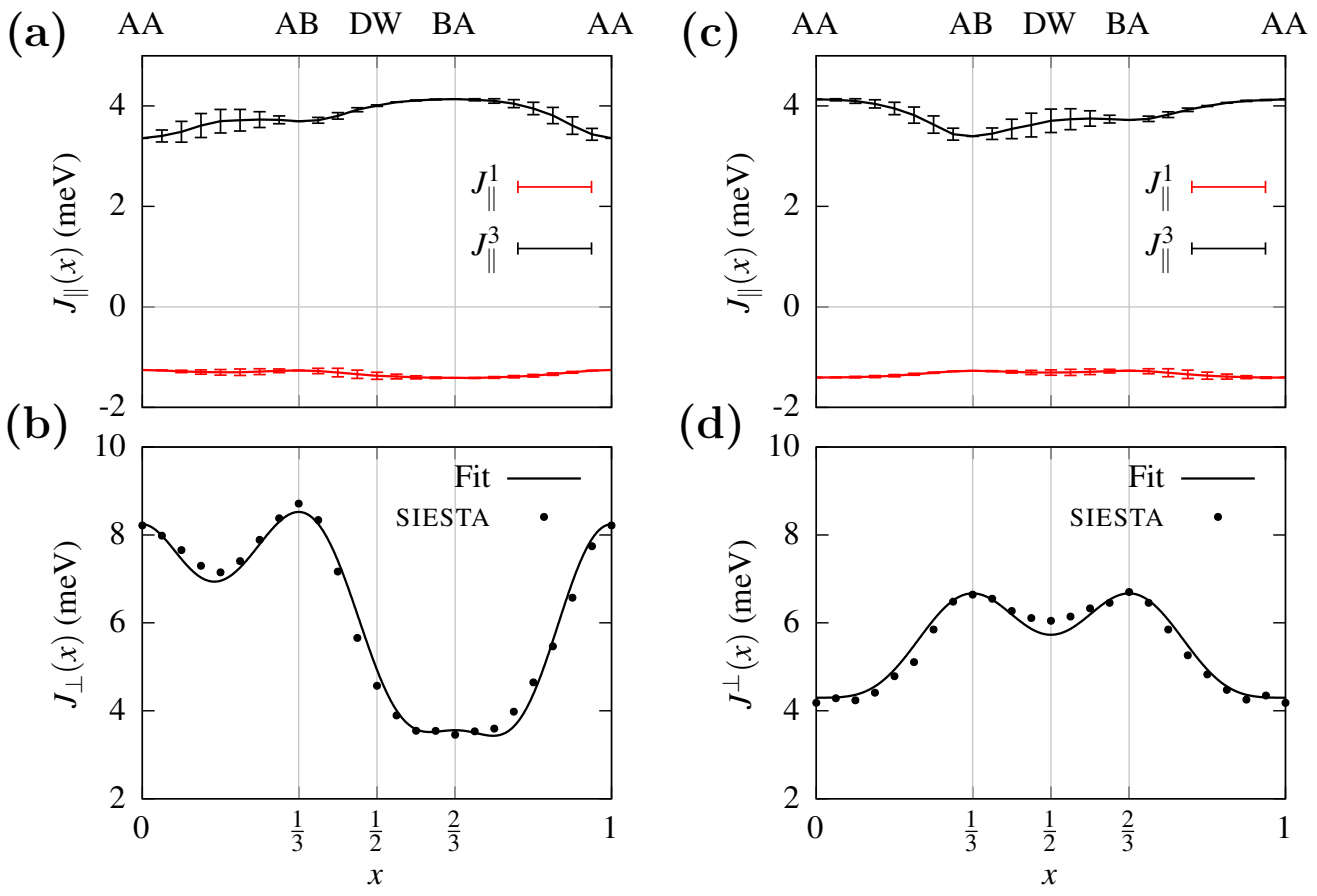

FIG. S5. Intralayer $J_\parallel$ and interlayer $J_\perp$ exchange as a function of stacking for **(a)**,**(b)** aligned and **(c)**,**(d)** anti-aligned bilayer NiI_2. In **(a)** and **(c)**, mean averages over the first ($J^1_\parallel$) and third nearest neighbors ($J^3_\parallel$) are shown, where the error bars indicate the corresponding mean square deviation. The points in **(b)** and **(d)** show the total energy differences from DFT calculations, the solid line was obtained using the fits to the stacking energy in Fig. 1 in the main text.

Fig. S6 shows the mean values of θ and z DM components in cylindrical coordinates for the first shell of NN atoms. These mean magnitudes reach values as large as 0.1 meV, corresponding to about $\sim 10\%$ of $J_{\parallel}^{1}$, which may alter the behavior of the different spin textures in the bilayer. We note that the angular component D^{θ} changes sign in the FM configurations as a function of stacking as shown in Figs. S6 (b) and (d). This conveys a change in the in-plane chirality of the DM vector, where $D^{\theta} > 0$ and $D^{\theta} < 0$ imply right- and left-handed chirality, respectively.

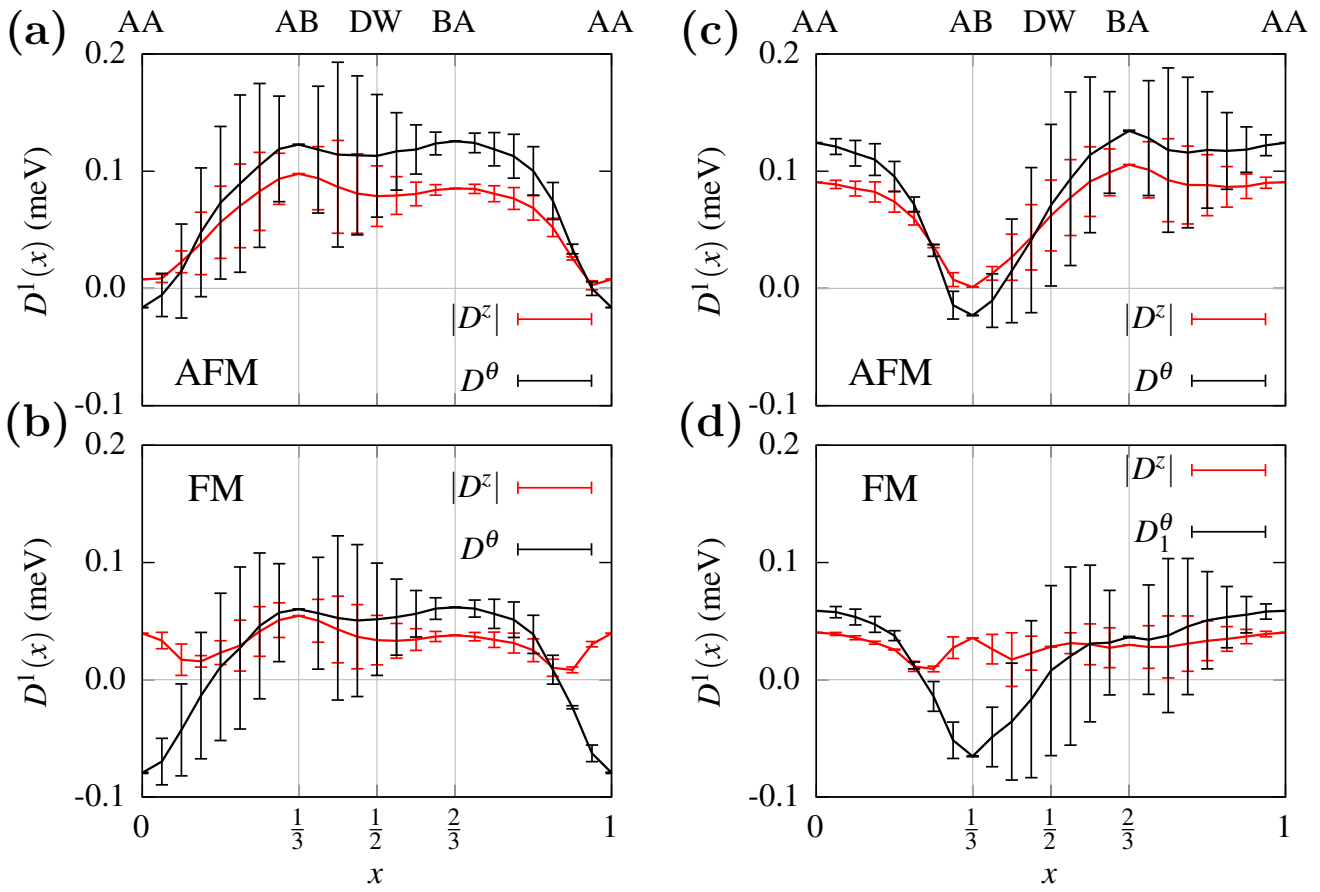

FIG. S6. Angular (θ) and z components of the first-neighbor DM vectors, averaged over the six neighbors for **(a)**,**(b)** aligned and **(c)**,**(d)** anti-aligned bilayer NiI_2. Choosing a cylindrical coordinate system where the radial component is oriented along each respective bond is more convenient because the radial components are all negligible, meaning that only the angular D^{θ} components need to be considered. The error bars show the mean square deviations. Note that D^{θ} and D^{z} respond differently to the change in relative stacking.

The intralayer magnetic exchange parameters for individual NNs are shown in Fig. S7, for aligned and anti-aligned stackings, as well as AFM and FM interlayer spin configurations. The exchange is shown for the six 1st NNs, which are linear combinations of the lattice vectors: $\mathbf{v}_n^1 = i\mathbf{a}_1 + j\mathbf{a}_2$ such that $\left|\mathbf{v}_n^1\right| = 1$. The indices (i, j) for $\mathbf{v}_n^1$ are, in order:

$$\mathbf{v}_1^1 = (0,1), \quad \mathbf{v}_2^1 = (1,0), \quad \mathbf{v}_3^1 = (-1,0), \quad \mathbf{v}_4^1 = (0,-1), \quad \mathbf{v}_5^1 = (1,-1), \quad \mathbf{v}_6^1 = (-1,1)\,. \tag{S5}$$

The exchange is also shown for the six 3rd NNs, where $\mathbf{v}_n^3 = 2\mathbf{v}_n^1$. There is a splitting between neighbors 1–4 and 5–6 as a function of relative stacking.

Fig. S8 shows the D^θ and $|D^z|$ components of the DM vector as a function of relative stacking, which also has a splitting between neighbors 1–4 and 5–6.

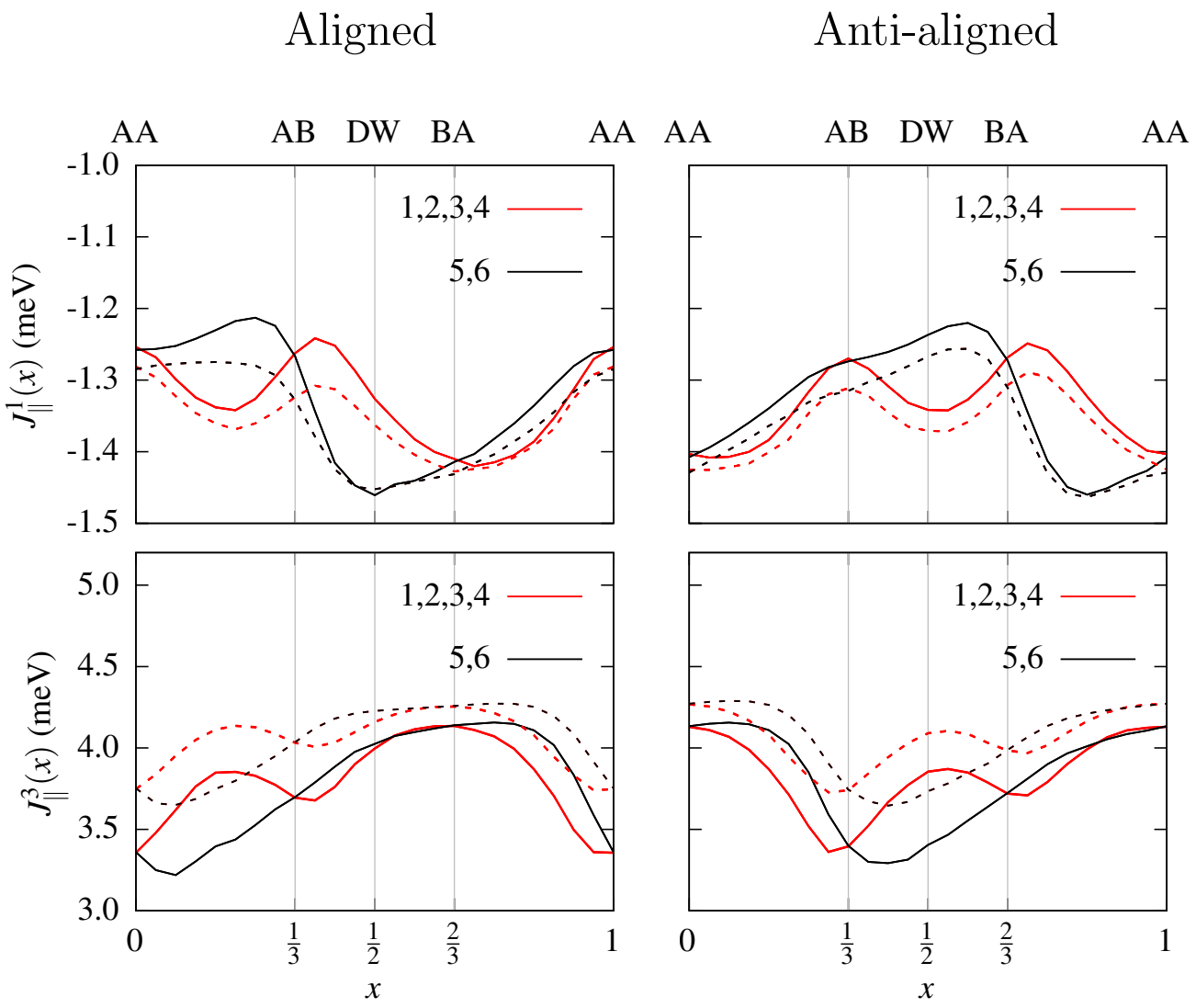

FIG. S7. 1st NN (top) and 3rd NN (bottom) intralayer exchange parameters as a function of relative stacking in aligned (left) and anti-aligned (right) bilayer NiI_2. The solid and dashed lines represent the AFM and FM interlayer spin order, respectively. Neighbors 1–4 are represented by the red lines, and neighbors 5–6 are represented by the black lines.

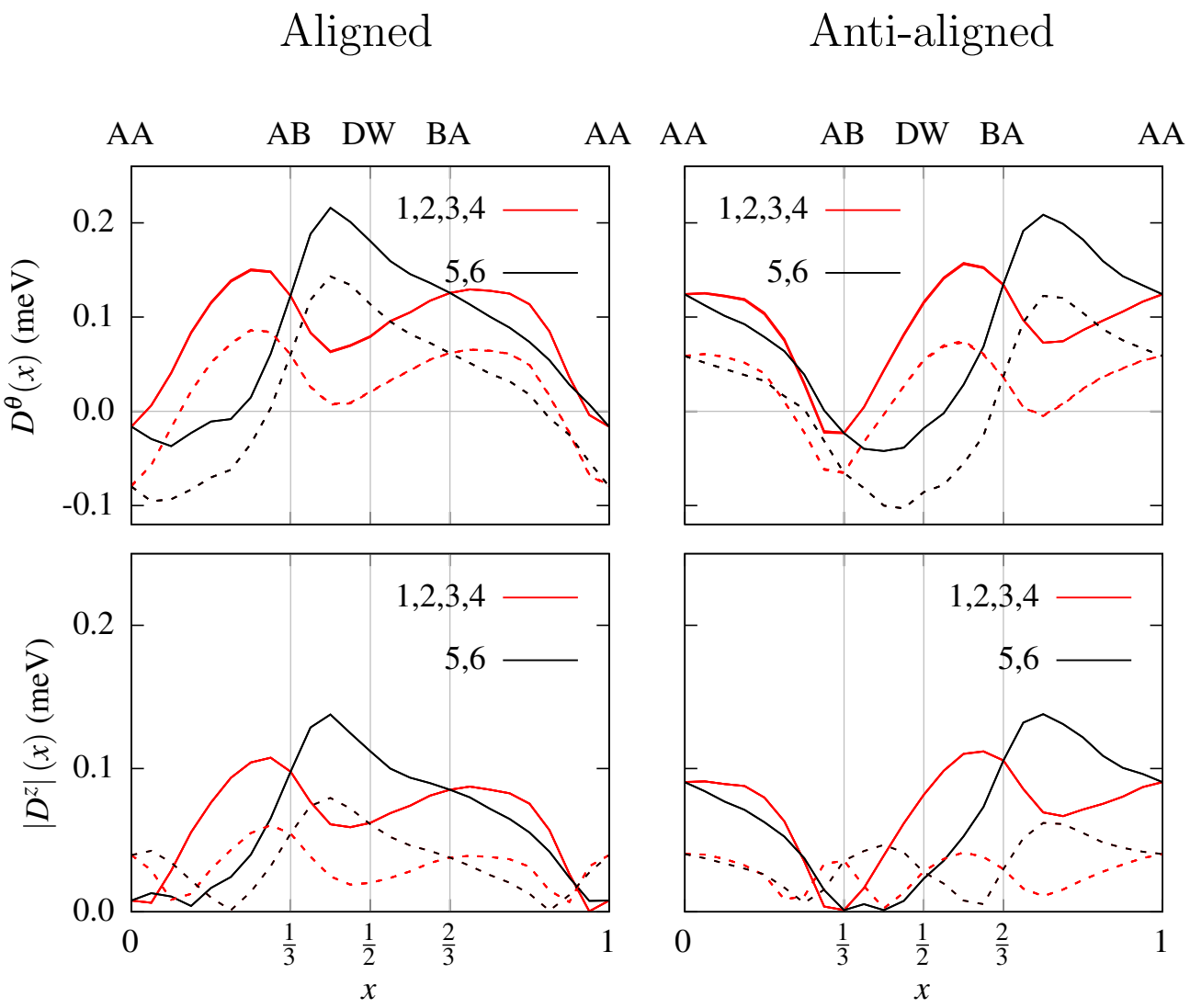

FIG. S8. D^θ (top) and $|D^z|$ (bottom) components of the DM vector as a function of relative stacking in aligned (left) and anti-aligned (right) bilayer NiI_2. The solid and dashed lines represent the AFM and FM interlayer spin order, respectively. Neighbors 1–4 are represented by the red lines, and neighbors 5–6 are represented by the black lines.

MONTE CARLO SPIN SIMULATIONS

MC simulations were performed using the Heisenberg model:

$$H = H_{\text{intra}} + H_{\text{inter}} - \sum_i \mathbf{B} \cdot \mathbf{S}_i \,, \tag{S6}$$

where H_{intra} and H_{inter} are given by Eqs. 3 and 4 in the main text, and the last term is the Zeeman interaction. The intralayer exchange parameters for monolayer NiI_2 from Ref. [11] were used, which were calculated using the supercell method, because the exchange parameters calculated using the LKAG method underestimate the intralayer exchanges (1^{st} NN in particular) due to the strong hybridization between the Ni and I atoms in each layer. The 1^{st}, 2^{nd} and 3^{rd} NN exchange parameters are $J_{\parallel}^{1} = -7.0$ meV, $J_{\parallel}^{2} = -0.3$ meV and $J_{\parallel}^{3} = +5.8$ meV, respectively. In addition, the anisotropic exchange parameters for the 1^{st} NNs between Ni atoms are taken into account. For the interlayer interaction, we take only the NN exchange parameter, and estimate that with the energy difference between the ferromagnetic and antiferromagnetic interlayer alignments, which gives a $J_{\perp} = 7$ meV. Calculations were repeated using the exchange parameters obtained in this work. The results using both sets of exchange parameters are compared in SM.

We then perform Metropolis MC simulations to estimate the magnetic field required to align the interlayer magnetic moments. The calculations are performed using a 64×64 supercell, with periodic boundary conditions in the in-plane directions. Calculations were repeated using a 128×128 supercell to check the convergence with respect to system size, see Fig. S9. The results are virtually identical, suggesting that results are sufficiently converged for a 64×64. An additional calculation using a 1×1 cell was performed so that intralayer interaction is constrained to be FM. We note that if the intralayer spin is constrained to be FM, the coercive magnetic field is much smaller, approximately 25 T with an in-plane magnetic field, which is consistent with the estimation from firs-principles calculations, or approximately 120 T with an out-of-plane magnetic field.

Monte Carlo spin simulations were performed using both the exchange values obtained in Ref. [11], and this work, see Fig. S10. The 1^{st}, 2^{nd} and 3^{rd} NN exchange parameters from this work are -1.7 meV, 0 meV and $+4.0$ meV, respectively. The interlayer exchange value used in both sets of calculations is $+7.0$ meV. Both sets of calculations yield qualitatively similar results, with small differences in the Néel temperature and coercive magnetic fields.

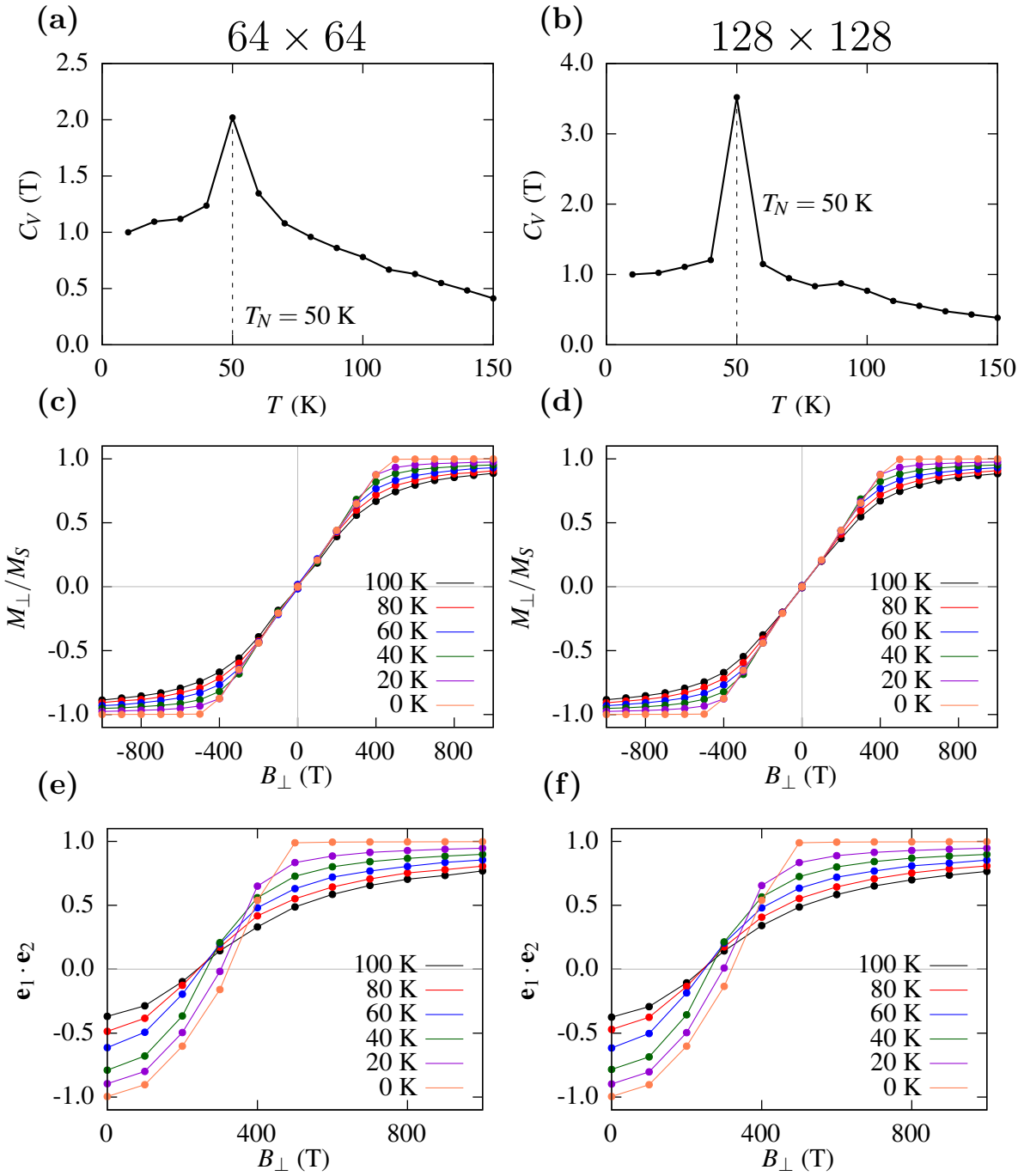

FIG. S9. **(a)–(b)** Specific heat C_V of the system as a function of temperature T from MC simulations for **(a)** a 64×64 supercell and **(b)** a 128×128 supercell. C_V is normalized such that $C_V(T \to 0) = 1$. **(c)–(d)** Magnetic moment as a function of perpendicular magnetic field $B_\perp$ and temperature, for **(c)** a 64×64 supercell and and **(d)** a 128×128 supercell. **(e)–(f)** Relative alignment between the spins in each layer, $\mathbf{e}_1 \cdot \mathbf{e}_2$ as a function of perpendicular magnetic field $B_\perp$ and temperature, for **(e)** a 64×64 supercell and **(f)** a 128×128 supercell.

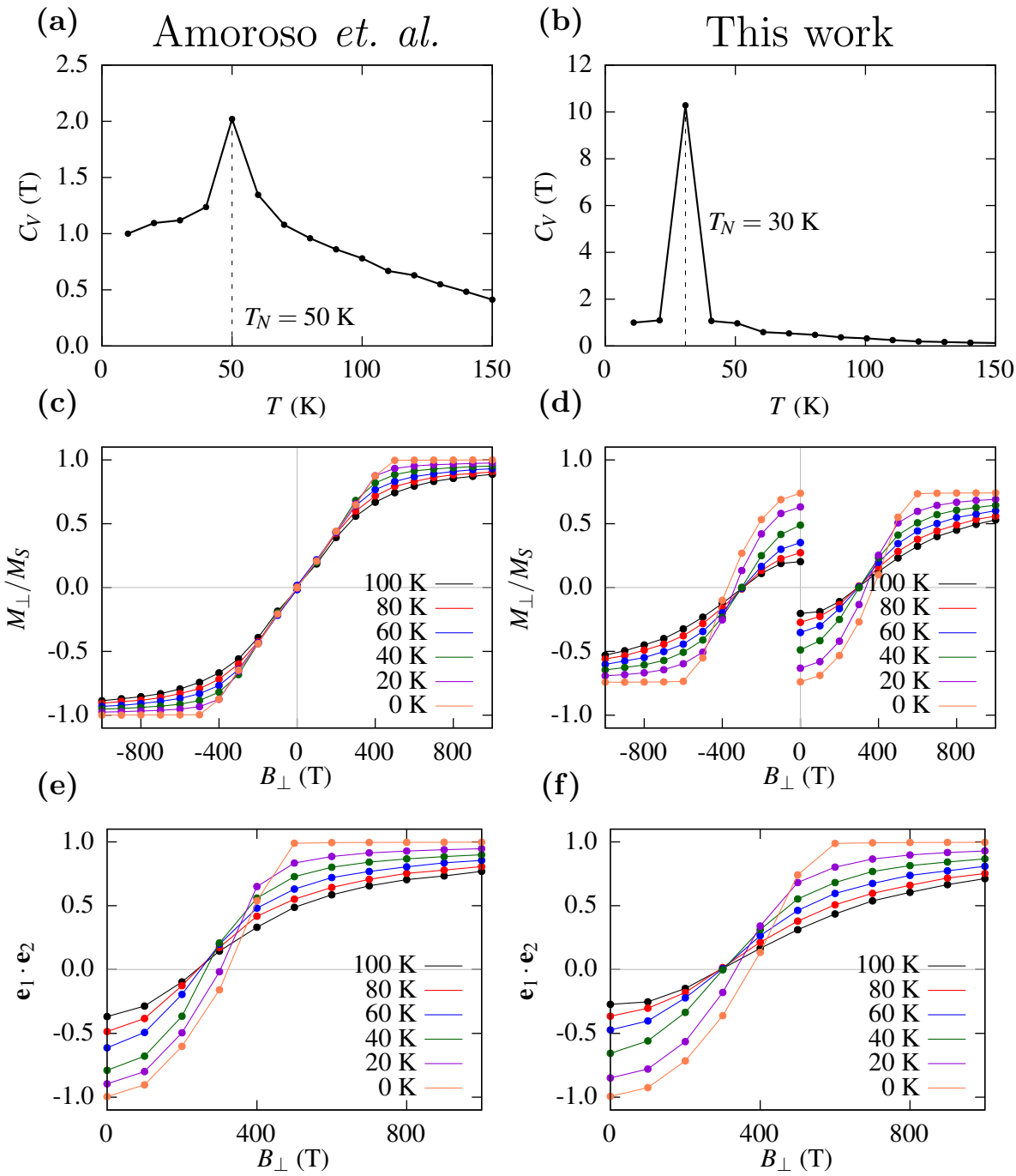

FIG. S10. **(a)–(b)** Specific heat C_V of the system as a function of temperature T from MC simulations for **(a)** Ref. [11] and **(b)** this work. C_V is normalized such that $C_V(T \to 0) = 1$. **(c)–(d)** Magnetic moment as a function of perpendicular magnetic field $B_\perp$ and temperature, for **(c)** Ref. [11] and **(d)** this work. **(e)–(f)** Relative alignment between the spins in each layer, $\mathbf{e}_1 \cdot \mathbf{e}_2$ as a function of perpendicular magnetic field $B_\perp$ and temperature, for **(e)** Ref. [11] and **(f)** this work.

COMPARISON WITH OTHER VAN DER WAALS FERROELECTRICS

The stacking-dependent out-of-plane dipole moment of anti-aligned bilayer NiI_2 is compared with other vdW ferroelectrics in Fig. S11, namely rhombohedral bilayer hBN and WSe_2. The dipole moment in NiI_2 is comparable or larger than those of hBN and WSe_2, depending on the interlayer spin configuration.

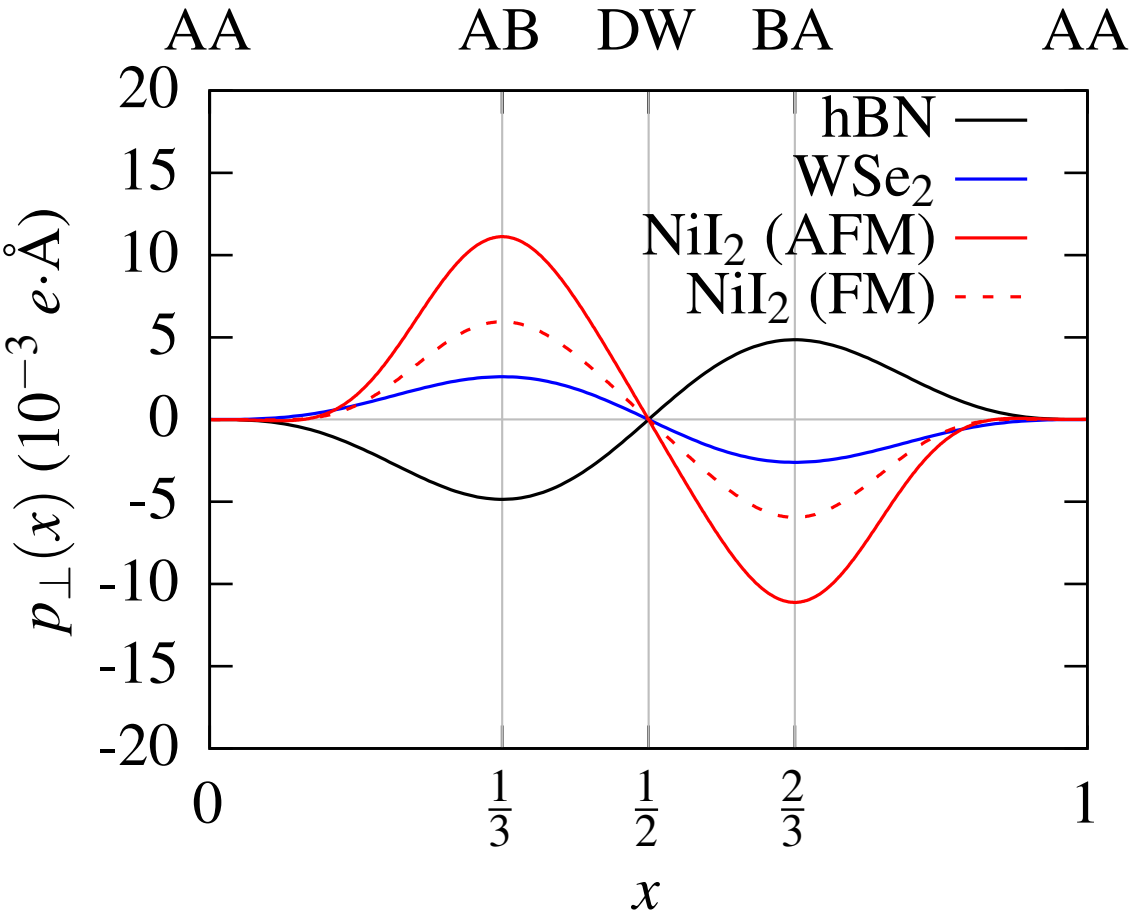

FIG. S11. Plot of the out-of-plane dipole moment as a function of stacking in bilayer hBN (black), WSe_2 (blue) and NiI_2 (red), for AFM (solid) and FM (dashed) interlayer spin configurations.

[1] J. M. Soler, E. Artacho, J. D. Gale, A. García, J. Junquera, P. Ordejón, and D. Sánchez-Portal, J. Phys. Condens. Matter **14**, 2745 (2002).
[2] D. Hamann, Phys. Rev. B **88**, 085117 (2013).
[3] A. García, M. J. Verstraete, Y. Pouillon, and J. Junquera, Comput. Phys. Commun. **227**, 51 (2018).
[4] M. Van Setten, M. Giantomassi, E. Bousquet, M. J. Verstraete, D. R. Hamann, X. Gonze, and G.-M. Rignanese, Comput. Phys. Commun. **226**, 39 (2018).
[5] N. R. Papior, G. Calogero, and M. Brandbyge, J. Phys.: Condens. Matter **30**, 25LT01 (2018).
[6] X. Gonze, B. Amadon, P.-M. Anglade, J.-M. Beuken, F. Bottin, P. Boulanger, F. Bruneval, D. Caliste, R. Caracas, M. Côté, *et al.*, Comput. Phys. Commun. **180**, 2582 (2009).
[7] H. J. Monkhorst and J. D. Pack, Phys. Rev. B **13**, 5188 (1976).
[8] J. P. Perdew, K. Burke, and M. Ernzerhof, Phys. Rev. Lett. **77**, 3865 (1996).
[9] S. Grimme, J. Antony, S. Ehrlich, and H. Krieg, J. Chem. Phys. **132** (2010).
[10] J. Neugebauer and M. Scheffler, Phys. Rev. B **46**, 16067 (1992).
[11] D. Amoroso, P. Barone, and S. Picozzi, Nat. Commun. **11**, 5784 (2020).
[12] M. J. Rutter, Comput. Phys. Commun. **225**, 174 (2018).
[13] D. Bennett, G. Chaudhary, R.-J. Slager, E. Bousquet, and P. Ghosez, Nat. Commun. **14**, 1629 (2023).
[14] G. Martínez-Carracedo, L. Oroszlány, A. García-Fuente, B. Nyári, L. Udvardi, L. Szunyogh, and J. Ferrer, Phys. Rev. B **108**, 214418 (2023).
[15] A. I. Liechtenstein, M. Katsnelson, V. Antropov, and V. Gubanov, J. Magn. Magn. Mater. **67**, 65 (1987).
[16] N. Sivadas, S. Okamoto, X. Xu, C. J. Fennie, and D. Xiao, Nano Lett. **18**, 7658 (2018).